# Two-Dimensional Group IV Monochalcogenides: Anode Materials for Li-Ion Batteries

Sharmistha Karmakar, Chandra Chowdhury, and Ayan Datta*

Department of Spectroscopy, Indian Association for the Cultivation of Science, 2A and 2B Raja S. C. Mullick Road, Jadavpur, Kolkata, West Bengal 700032, India

S *Supporting Information*

ABSTRACT: The selection of a suitable electrode material is a fundamental step in the development of Li-ion batteries (LIBs) to achieve enhanced performance. In the present study, we have explored the feasibility of monolayers of phosphorene analogues, namely, group IV monochalcogenides (SiS, SiSe, GeS, GeSe, SnS, and SnSe), to serve as anode materials in LIBs by density functional theory (DFT). Our exploratory study indicates that lithium binds efficiently to these monolayers, with Li@SiS and Li@SiSe showing appreciable stability comparable to that of phosphorene. The zero-point-energy-corrected minimum-energy pathway (MEP) for Li diffusion demonstrates high anisotropy for both SiS and SiSe, with a low diffusion barrier of ~0.15 eV along the zigzag direction. Inclusion of corrections due to quantum effects such as the zero-point energy (ZPE) and quantum mechanical tunneling (QMT) increases the diffusion rates by 6−10% at room temperature and results in increasingly significant contributions as the temperature is reduced (40−55% increment at T = 100 K). The calculated theoretical capacities for SiS and SiSe are 445.7 and 250.44 mA h g^{-1}, respectively, which are well above those of existing commercially available anode materials. Both SiS and SiSe preserve their structural integrity upon lithiation, justifying their role as host materials for lithium. A semiconductor → metallic transition is observed upon full lithiation for both materials. All of these exceptional properties, including low diffusion barrier, moderate to high specific capacity, low open-circuit voltage (OCV), small volume change, and good electrical conductivity, suggest that monolayer SiS and SiSe could serve as promising electrode materials in LIBs.
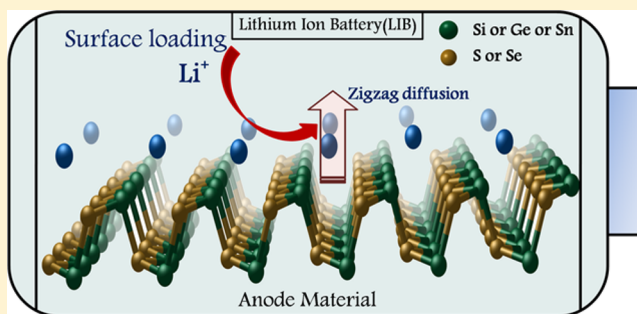
INTRODUCTION

The ever-increasing demand for fossil fuel has led to the discovery of many alternative sources of energy, among which the lithium-ion battery (LIB) is highly promising.[1−3] The high reversible capacities, high power densities, and long cycle lives makes LIBs suitable candidates for portable and "green" energy-storage materials.[4−6] However, the performance of LIBs is strongly controlled by the choice of electrode materials (cathode and anode)[7,8] and electrolyte.[9] Among carbon-based materials, graphite has been extensively used as an anode material in LIBs.[10,11] However, a poor specific capacity (372 mA h g^{-1}) limits its application in modern electronics.[3] Moving from graphite to its two-dimensional analogue, graphene, leads to a high predicted specific capacity of ~955 mA h g^{-1}.[5,12,13] Unfortunately, a high diffusion barrier and lithium nucleation over graphene limit its application in terms of durability.[14] Anode materials based on silicon, the next alternative to carbon, provide a very high theoretical capacity of 4212 mA h g^{-1} owing to Li alloy formation.[15,16] However, these materials tend to degrade as a result of large volume changes.[17,18] Silicene, the two-dimensional Si-based counterpart of graphene, forms a buckled layered structure as a result of puckering in the hexagonal Si_6 rings due to pseudo-Jahn−Teller (PJT)

distortion.[19−21] It has been shown theoretically that pristine silicene and silicene supported on MgX_2 are promising candidates for the negative electrode in Li-ion batteries.[22,23] Various other two-dimensional materials such as MXenes and layered transition metal dichalcogenides have also been widely studied for this purpose.[24,25] Such new two-dimensional materials exhibit unusual chemical bonding characteristics and stoichiometries and could structurally mimic graphene monolayers.[26−28]

Black phosphorus, the thermodynamically most stable allotrope of phosphorus,[29] is, like graphite, a layered material and is known to have a large theoretical capacity of 2596 mA h g^{-1}.[30,31] However, its poor cycle life and irreversible structural changes limit its application as the negative electrode in LIBs.[32] Recently, phosphorene, the two-dimensional analogue of black phosphorus, and phosphorene-based hybrid materials have shown great potential as anode materials in Li-ion batteries.[33,34] However, high reactivity of phosphorene toward O_2 and H_2O still poses significant technological

bottlenecks.[35] Recently, we showed that application of a capping layer of hexagonal boron nitride (*h*-BN) enhances the performance of black phosphorene as an anode material.[36] Indeed, the search for optimal electrode materials is still in its infancy, and several aspects must be considered in the design of new anode materials.

The two-dimensional analogues of group IV monochalcogenides, MX (M = Si, Ge, or Sn; X = S or Se), display a structural similarity to phosphorene and form buckled honeycomb lattices.[37,38] The basic hexagonal ring structure of these systems consist of a puckered M_3X_3 unit similar to the P_6 unit of phosphorene in which each sp^3-hybridized M/X atom is covalently linked to three adjacent X/M atoms exhibiting a characteristic wavelike structure.[37] The bulk form of these four monochalcogenides (GeS, SnS, GeSe, and SnSe) is known to exist in an orthorhombic crystal structure similar to that of black phosphorus. They belong to space group *Pcmn* (D_{2h}^{16}), whereas the space group of black phosphorus is *Bmab* (D_{2h}^{18}), as it consists of only one element.[37] Preparation of monolayers of the monochalcogenides either by exfoliation from the bulk material or by other chemical processing (see Scheme 1) is an

Scheme 1. Proposed Synthesis of Free-Standing Monolayers of MX, where M = Si, Ge, or Sn and X = S or Se, Using Physical Techniques Such as Sonication and Mechanical Exfoliation or Chemical Techniques Such as Intercalation by Ionic Liquids or Ions
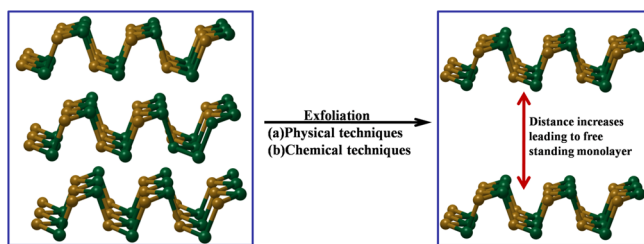
active area of research.[39,40] Recently, silicon monosulfide and monoselenide were predicted to form stable free-standing monolayers similarly to phosphorene, and therefore, synthesis of *α*-SiS and *α*-SiSe monolayers is highly feasible through different efficient deposition techniques.[38,41] All of these materials are semiconductors with direct or indirect band gaps ranging from 0.96 to 1.65 eV.[37,38] The similarities in structure and electronic properties make their properties analogous. Additionally, nanostructured germanium and tin chalcogenides (GeS, GeSe, SnS, and SnSe) are known to be good anode materials in rechargeable lithium-ion batteries.[42] Although a high theoretical capacity is the main advantage of these nanostructured materials, large volume changes owing to the formation of Li alloys (such as $Li_{4.4}Ge$ and $Li_{4.4}Sn$) during lithiation limit their performance.[42,43] Lithium silicon sulfide (Li_2SiS_3) has also been used as a negative electrode in solid-state lithium batteries.[44] However, the feasibility of their monolayers for Li storage materials is still unexplored.

The performance of LIBs also depends on the Li diffusion barrier, and a high charging/discharging rate is extremely desirable to achieve fast switching results. Therefore, a small barrier for Li hopping between the various possible sites is highly desirable. In this work, using first-principles calculations, we have investigated the suitability of two-dimensional group IV monochalcogenides as host materials in LIBs. We have identified the favorable binding sites for Li and the minimum-

energy pathways (MEPs) for diffusion. Our results show that both SiS and SiSe monolayers have excellent potential to perform as negative electrodes in LIBs. Additionally, because lithium is the third lightest element in the periodic table, it should have a non-negligible contribution from quantum mechanical tunneling (QMT). In fact, Li is one-half the mass of carbon, and carbon has been shown to have interesting signatures of heavy-atom tunneling.[45−47] In this work, we consider both QMT and zero-point-energy (ZPE) effects in the context of LIBs for these systems using the one-dimensional Wigner correction,[48,49] which takes into account both quantum effects, to provide a more accurate estimate of the activation energies.

■ COMPUTATIONAL DETAILS

All electronic structure calculations were performed using density functional theory (DFT) as implemented in the Quantum Espresso package.[50] The electron−ion interactions were described by an ultrasoft pseudopotential,[51] whereas the electron exchange-correlation interactions were treated by the generalized gradient approximation (GGA) of the Perdew−Burke−Ernzerhof (PBE) approach.[52] A kinetic energy cutoff of 40 Ry was used for all calculations. Structural relaxations were carried out using the Broyden−Fletcher−Goldfarb−Shanno (BFGS) quasi-Newton algorithm[53] until convergence criteria of 10^{-5} eV for energy and 0.01 eV/Å for force were reached. van der Waals interactions were taken into account by the semiempirical correction scheme of Grimme (DFT-D2),[54] which is known to give an accurate description of the Li binding energy and diffusion barrier. A vacuum space of about 20 Å was employed between two adjacent layers to avoid spurious interactions induced by periodic images. The Brillouin zone was represented by a Monkhorst−Pack special *k*-point mesh of 5 × 5 × 1 for structural relaxation. The minimum-energy path (MEP) for Li diffusion was located using the climbing-image nudged-elastic-band (CI-NEB) method.[55] Eight intermediate images were generated by linear interpolation between the initial and final states along the reaction coordinate, and then these images were relaxed until the largest norm of the force orthogonal to the path was smaller than 0.01 eV/Å. The charge transfer between the Li atoms and MX monolayers was modeled using Bader charge analysis software.[56]

Calculations of the band structures, densities of states (DOS), and phonon frequencies were carried out using projector-augmented-wave (PAW) potentials[57] based on density functional theory (DFT-D2) as implemented in the Vienna ab initio simulation package (VASP) code,[58] and the exchange-correlation energy was obtained using the GGA-PBE approximation. The energy convergence criterion was chosen to be 500 eV, and the *k*-point mesh was 7 × 7 × 1. The imaginary frequency of the transition state (TS) along the diffusion coordinate was obtained at the Γ point only by means of phonon frequency calculations using density functional perturbation theory (DFPT), resulting 3*N* − 3 real frequencies for the reactant and 3*N* − 4 real frequencies and 1 imaginary frequency for the TS, as required for Wigner corrections to the classical barrier.

■ RESULTS AND DISCUSSION

The ability of an anode material to bind Li determines its capacity in Li-ion batteries. Stronger binding indicates more

storage of Li atoms and, hence, a higher capacity. When the binding energy of Li to the host surface is less than its bulk cohesive energy (1.63 eV),[59] the formation of lithium clusters is thermodynamically favorable. It is well-known that weak lithium binding over defect-free graphene causes dendritic Li growth, which eventually leads to explosion hazards,[3,14] limiting the application of defect-free graphene in battery technology. Hence, the Li binding energy (E_b) to the MX monolayers is an important parameter for determining the ability of MX monolayers to perform as anode materials.

The adsorption energy per Li atom can be written as[33]

$$E_b = (E_{MX} + nE_{Li} - E_{MX+nLi})/n$$

where E_{MX+nLi} is total energy of a pristine MX layer containing n Li atoms, E_{MX} is the energy of an MX monolayer, E_{Li} is the energy of an isolated Li atom, and n is the number of Li atoms adsorbed. To evaluate E_b, we used a 3 × 3 monolayer of MX containing one Li atom. A larger positive value of E_b indicates stronger binding to the surface. We considered all possible binding sites for Li adsorption and found the hollow sites, namely, H_1 and H_2, to be the most probable sites where the Li atom is coordinated to three atoms. Figure 1 shows the various
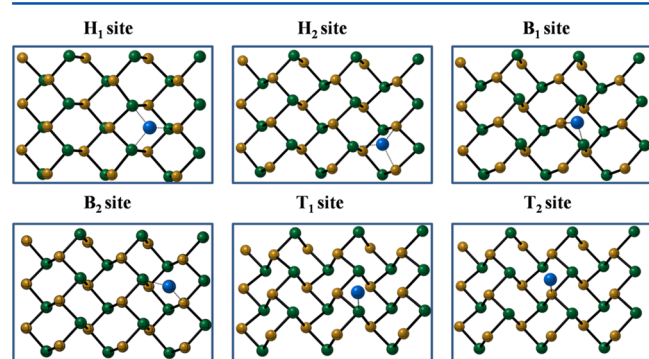

Figure 1. Top view of different stable Li adsorption sites on SiX (X = S or Se). Color code for atoms: green, Si; orange, X (S, Se); blue, Li.

binding sites of Li on the hosts. In the H_1 site, Li is coordinated to two M atoms and one X atom, whereas for the H_2 site, the coordination patterns are reversed. Table 1 lists the binding

Table 1. Binding Energies (E_b, eV) and Amounts of Charge Transfer (Q_{Li}) Calculated at Sites H_1 and H_2 for MX Systems

	site H_1		site H_2	
MX	$E_b{}^a$ (eV)	Q_{Li}	$E_b{}^a$ (eV)	Q_{Li}
SiS	1.85 (2.34)	0.99	1.71 (2.3)	0.99
SiSe	1.96 (2.24)	0.99	1.94 (2.26)	0.99
GeS	1.04 (1.86)	0.99	1.09 (2.03)	0.99
GeSe	1.02 (1.93)	0.99	1.05 (1.96)	0.99
SnS	0.97 (1.90)	0.99	1.07 (2.05)	1.00
SnSe	1.20 (2.15)	1.00	1.24 (2.21)	1.00

^{a}Data in parentheses obtained from VASP calculations with the same geometry using the PAW pseudopotential.

energies (E_b) and amounts of charge transfer (Q_{Li}) at the H_1 and H_2 sites. The data in parentheses (see Table 1) were obtained from VASP calculations with the same geometry using the PAW pseudopotential.

From Table 1, it can be seen that all of the monolayers have encouraging Li binding energies, with those of SiS and SiSe

being highest. In fact, the adsorption energies of Li to SiS and SiSe are similar to that of black phosphorene.[33] Table 1 shows that the amount of charge transfer (CT) ranges from 0.99 to 1.00 e in all cases; hence, the Li atom exists in a cationic state after adsorption onto the MX monolayers, and Coulomb forces account for the stabilization of Li on the MX layers. The Coulomb interactions are directly proportional to (1) the amount of charge transfer between Li and the MX layer; (2) the amount of fractional charge present on the M−X bond, which results from the difference in the electronegativities of M and X; and (3) the distance between the coordinated atoms (d_{Li-M} or d_{Li-X}). Hence, the shorter bonding distance and larger polarization in the Si−X bond for X = S and Se facilitate stronger Li adsorption than for the other group IV chalcogenides. However, because of the heavier mass of the latter analogues (GeS, GeSe, SnS, and SnSe), the expected specific capacities should be low irrespective of a high binding energy towards Li. Hence, we selected the previously uninvestigated SiS and SiSe monolayers for further calculations to validate their suitability as anode materials in LIBs.

To explore the binding interactions of Li with SiS and SiSe monolayers, it is important to determine the possible Li adsorption sites. The structural asymmetry in SiS and SiSe results in six different binding positions, which can be described as follows: (1) above the center of the SiS hexagon coordinating to two Si and one X atoms (H_1 site), (2) above the center of the SiS hexagon coordinating to one Si and two X atoms (H_2 site), (3) above the midpoint of the Si−X bond located near Li (B_1 site), (4) above the midpoint of the Si−X bond located far from Li (B_2 site), (5) on the top of Si (T_1 site), and (6) on the top of X (T_2 site). They are shown in Figure 1. Table 2 summarizes the calculated binding energies

Table 2. Binding Energies (E_b, eV) and Li−Si and Li−X Bond Lengths (d_{Li-Si} and d_{Li-X}, Å) at Different Adsorption Sites for SiS and SiSe

	SiS		SiSe	
adsorption site	E_b (eV)	d_{Li-Si}, d_{Li-S} (Å)	E_b (eV)	d_{Li-Si}, d_{Li-Se} (Å)
H_1	1.85	2 × d_{Li-Si} = 2.64, d_{Li-S} = 2.49	1.96	2 × d_{Li-Si} = 2.65, d_{Li-Se} = 2.60
H_2	1.71	d_{Li-Si} = 2.65, 2 × d_{Li-S} = 2.59	1.94	d_{Li-Si} = 2.59, 2 × d_{Li-Se} = 2.67
B_1	1.07	d_{Li-Si}, d_{Li-S} = 2.65	1.11	d_{Li-Si}, d_{Li-Se} = 2.60
B_2	1.49	d_{Li-Si}, d_{Li-S} = 2.55	1.87	d_{Li-Si}, d_{Li-Se} = 2.60
T_1	0.96	2.6	1.03	2.5
T_2	1.03	2.5	0.88	2.5

(E_b) and other structural parameters for the different adsorption sites. As discussed above, for the hollow sites (H_1 and H_2), Li is coordinated to three neighboring atoms. However, for sites B_1/B_2 and T_1/T_2, the coordination numbers are two and one, respectively. For both SiS and SiSe, the hollow sites are most stabilizing for Li. Whereas H_1 is the most stable adsorption site for SiS, for SiSe, the two hollow sites (H_1 and H_2) share similar binding energies. Hence, we can conclude that the Li atom favors binding sites that provide the maximum coordination number.

A high charging/discharging rate is highly desirable for the efficient performance of LIBs, which, in turn, is controlled by facile Li motion over the surface. We investigated different possible diffusion pathways and their corresponding barriers for Li migration over SiS and SiSe. Structural asymmetry results in
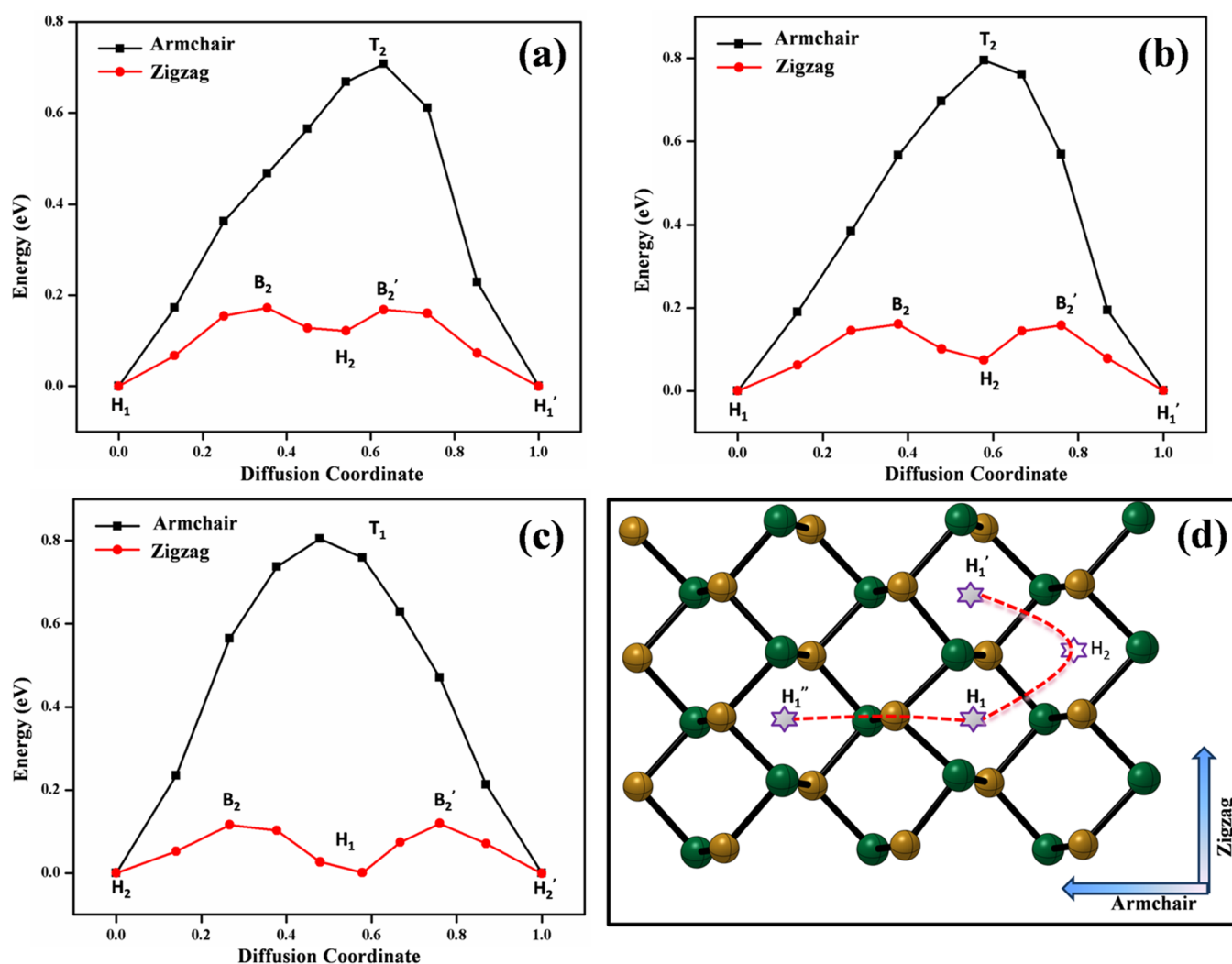
Figure 2. (a−c) Energy profiles for Li diffusion along the armchair and zigzag directions for (a) SiS ($H_1 \rightarrow H_1{}'$), (b) SiSe ($H_1 \rightarrow H_1{}'$), and (c) SiSe ($H_2 \rightarrow H_2{}'$). (d) Schematic representation of different Li diffusion pathways in SiX for the H_1 site.

two distinct diffusion paths, one along the zigzag direction (where Li moves in the same lane) and the other along the armchair direction (where Li hops from one lane to another). For SiS, as H_1 is the most stable adsorption site, the Li atom hops between neighboring H_1 sites. The energy profiles for Li migration over SiS are summarized in Figure 2a. The diffusion barriers were estimated to be 0.17 and 0.71 eV along zigzag and armchair direction, respectively. Along the zigzag direction, the Li atom resides at a B_2 site in the transition state, whereas T_2 serves as the transition-state structure in the armchair direction. Because the B_2 site has a higher binding energy than the T_2 site, the diffusion barrier height is lower along the zigzag direction. Therefore, the zigzag direction is predicted to be the most suitable diffusion pathway for Li over SiS.

For SiSe, the H_1 and H_2 sites have similar binding energies, and hence, a total of four (two for each site) diffusion directions are possible, as shown in Figure 2b,c. The calculated hopping barriers are 0.79 and 0.80 eV along the armchair directions for H_1 and H_2 sites, respectively. However, along the zigzag direction, the barriers are estimated to be 0.16 and 0.12 eV for H_1 and H_2 site, respectively. The Boltzmann population factor for the H_2 site relative to the H_1 site was found to be 0.46. Hence, at room temperature, 54% of the Li atoms occupy H_1 sites, and the rest reside at H_2 sites. The Boltzmann average

diffusion barrier was found to be 0.14 eV along the zigzag pathway. In both SiS and SiSe, the diffusion is quasi-one-dimensional along the zigzag direction and a sufficiently low barrier ensures high rate performance compared to other commercial anodes.

Next, we calculated the classical and quantum diffusion rates by incorporating the effects of zero-point energy (ZPE) and quantum mechanical tunneling (QMT) into the potential energy surface for Li hopping. Given that lithium is significantly less heavy than the atoms on the host surface such as Si, S, and Se, it is expected to exhibit substantial quantum mechanical effects which might consequently alter its diffusion kinetics.[60−62] According to transition-state theory (TST), the classical rate constant for ion diffusion within the harmonic approximation for vibrational modes can be written as[63,64]

$$k_{cl}^{hTST} = \frac{k_B T}{h} \frac{Q^{TS}}{Q^{IS}} e^{-\Delta E^{\ddagger}/k_B T}$$

(1)

where h is Planck's constant; k_B is the Boltzmann constant; T symbolizes temperature; and Q^{TS} and Q^{IS} represent the partition functions for the transition state and the initial state, respectively. In eq 1, $\Delta E^{\ddagger}$ is the classical barrier height and is obtained as the energy difference between the transition state
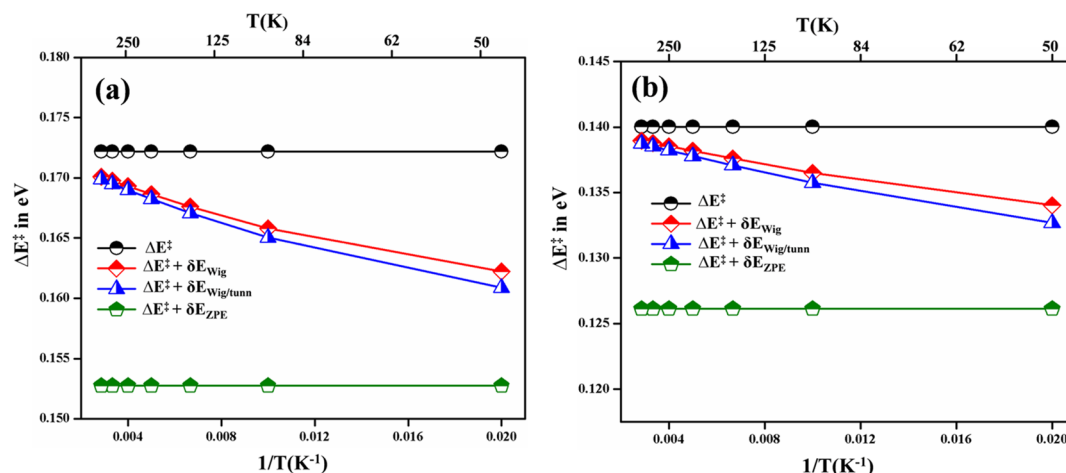
Figure 3. Variation of the diffusion barrier with respect to temperature for (a) SiS and (b) SiSe.

and the ground (initial) state as available from typical electronic structure calculations such as the NEB method without ZPE corrections. The ratio of partition functions is given by

$$\frac{Q_{TS}}{Q_{IS}} = \frac{h}{k_B T} \times \frac{\prod_i^{3N-6} \nu_i^{IS}}{\prod_i^{3N-7} \nu_i^{\ddagger}} \qquad (2)$$

where ν_i^{IS} and $\nu_i^{\ddagger}$ represent the vibrational frequencies of the IS and TS, respectively. The zero-point-energy correction (δE_{ZPE}) to the classical barrier height can be written as

$$\delta E_{ZPE} = \sum_i \frac{h\nu_i^{\ddagger}}{2} - \sum_i \frac{h\nu_i^{IS}}{2} \qquad (3)$$

where the first term is the total ZPE of the TS and the second term represent the total ZPE of IS. It is known that the ZPE-corrected barrier ($\Delta E + \delta E_{ZPE}$) is more accurate only at low temperature when all of the vibrational modes are in their ground states. However, in the intermediate temperature range relevant for the room-temperature description of materials, the Wigner correction[48] describes the barrier height more accurately. In this approximation, the quantum mechanical partition functions are used for vibrational modes, and their classical mechanical description is kept constant. The Wigner zero-point correction to the classical barrier height can be formulated as[48]

$$\delta E_{Wig} = -k_B T \ln\left[\frac{\prod_i \sinh(x_i^{IS})/x_i^{IS}}{\prod_i \sinh(x_i^{\ddagger})/x_i^{\ddagger}}\right] \qquad (4)$$

where $x_i^{IS/\ddagger} = h\nu_i^{IS/\ddagger}/2k_B T$, the ratio of the ZPE to the thermal energy at each vibrational mode. The quantum mechanical tunneling effect on the barrier height was also employed through the Wigner tunneling correction.[49]

Figure 3a,b shows the variations with temperature of the classical barrier ($\Delta E^{\ddagger}$), the ZPE-corrected barrier ($\Delta E^{\ddagger} + \delta E_{ZPE}$), the Wigner ZPE-corrected barrier ($\Delta E^{\ddagger} + \delta E_{Wig}$), and the Wigner ZPE- and tunneling-corrected barrier ($\Delta E^{\ddagger} + \delta E_{Wig/tunn}$) for SiS and SiSe in the temperature range of $T = 50-350$ K. It was found that the ZPE correction lowers the classical barrier height by 0.02 eV for SiS and by 0.014 eV for SiSe in the zigzag direction. The Wigner ZPE-corrected barrier ($\Delta E^{\ddagger} + \delta E_{Wig}$) lies between the classical barrier ($\Delta E^{\ddagger}$) and the ZPE-corrected barrier ($\Delta E^{\ddagger} + \delta E_{ZPE}$) in the intermediate temperature range. However, it approaches the $\Delta E^{\ddagger} + \delta E_{ZPE}$

value (green line) in the low-temperature limit and the $\Delta E^{\ddagger}$ value (black line) in the high-temperature limit. The temperature dependences of the Wigner ZPE-corrected barrier ($\Delta E^{\ddagger} + \delta E_{Wig}$) and the Wigner ZPE- and tunneling-corrected barrier ($\Delta E^{\ddagger} + \delta E_{Wig/tunn}$) are almost superimposed at high temperatures, indicating that QMT plays a minor role at room temperature ($\Delta E^{\ddagger} + \delta E_{Wig/tunn} \approx \Delta E^{\ddagger} + \delta E_{Wig}$). At 300 K, the classical barrier height is almost the same as the ZPE- and tunneling-corrected barrier, and the quantum correction lowers the barrier by only 2.7 meV for SiS and 1.5 meV for SiSe. However, as the temperature is reduced, $\Delta E^{\ddagger} + \delta E_{Wig/tunn} < \Delta E^{\ddagger}$, and as a result, the effective barrier (activation energy) decreases. This is corroborated by the calculations for the Li diffusion rates at 300 K with and without QMT corrections, as summarized in Table 3.

Table 3. Classical Diffusion Constants (k), Wigner ZPE- and Tunneling-Corrected Diffusion Constants ($k_{Wig/tunn}$), and Percentages of Tunneling at Three Different Temperatures (T = 100, 200, and 300 K) for SiS and SiSe

T (K)	k (s^{-1})	$k_{wig/tunn}$ (s^{-1})	QMT (%)
	SiS		
100	2.50×10^4	5.74×10^4	56.4
200	5.47×10^8	6.87×10^8	20.4
300	1.53×10^{10}	1.69×10^{10}	9.8
	SiSe		
100	3.79×10^5	6.21×10^5	39.0
200	1.28×10^9	1.45×10^9	12.0
300	1.92×10^{10}	2.03×10^{10}	5.6

The calculated classical diffusion constants are 1.53×10^{10} and 1.92×10^{10} s^{-1} for SiS and SiSe, respectively. The diffusion constants including corrections for zero-point energy and tunneling are 1.69×10^{10} and 2.03×10^{10} s^{-1} for SiS and SiSe, respectively, with an effective enhancement of 6−10% at room temperature. However, at 100 K, QMT boosts the diffusion rates by as much as 39% and 56% for SiSe and SiS, respectively.

We evaluated the Li storage capacity and open-circuit voltage by varying the Li content on SiS and SiSe monolayers. We considered a 3 × 2 supercell of SiS/SiSe and varied the number of Li atoms from 1 to 12 to generate different configurations of the stoichiometry Li$_m$SiX where m = 0.083, 0.17, 0.33, 0.67, and 1. In each case, we chose the most stable adsorption site for
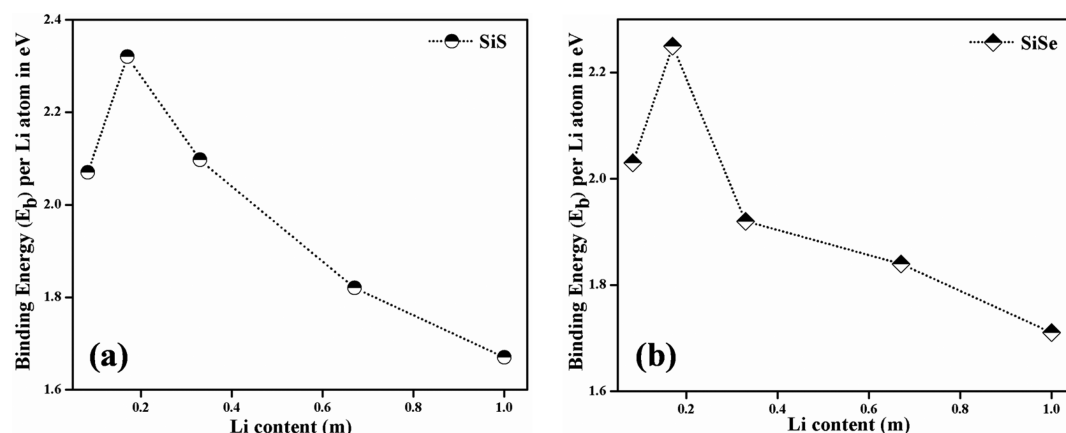
Figure 4. Binding energy (E_b) vs Li content (m) for (a) SiS and (b) SiSe.
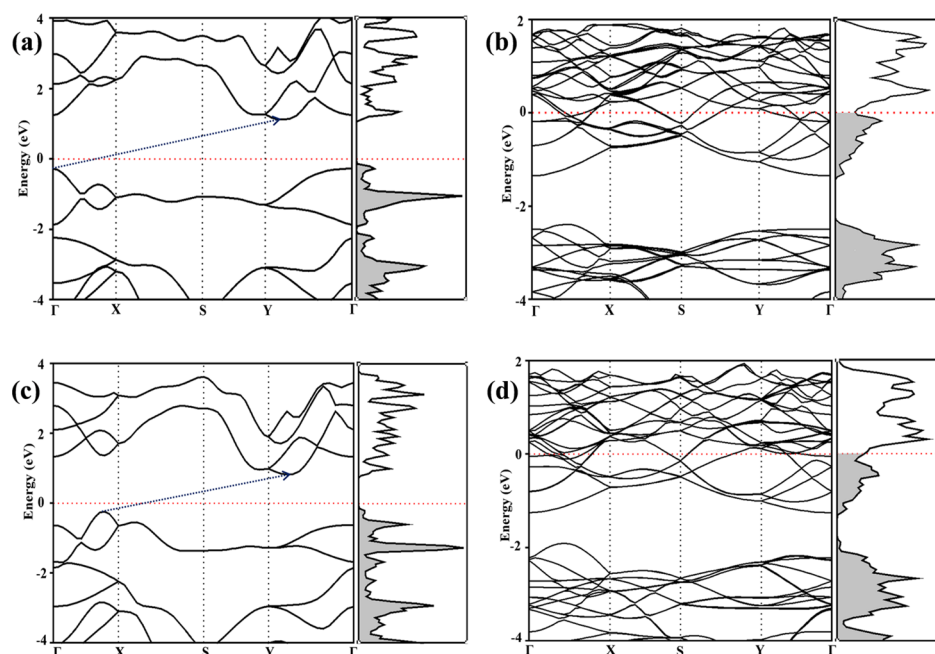

Figure 5. Electronic band structures and densities of states (DOS) for (a) pristine SiS, (b) fully lithiated SiS, (c) pristine SiSe, and (d) fully lithiated SiSe.

calculation and placed the Li at both sides (top and bottom) of the monolayer. Figure S1 shows the structures of SiS and SiSe at various concentrations of lithiation. Figure 4a,b shows the variation of the binding energy (E_b) with the Li content (m) for both SiS and SiSe. For both systems, the binding energy first increases from $m = 0.083$ to 0.17 and then gradually decreases with increasing m. This is because, as the Li content increases, the distance between neighboring Li atoms decreases, and this results in greater electrostatic repulsion, resulting in a lower E_b. When both the volume and entropy effects are neglected, the open-circuit voltage can be obtained at each value of m using the equation[65]

$$\text{OCV} \approx \frac{E_{\text{Li}_m\text{SiX}} - E_{\text{SiX}} - nE_{\text{Li}}}{-ne} \qquad (5)$$

where $E_{\text{Li}_m\text{SiX}}$ and E_{SiX} represent the total energies of lithiated and nonlithiated 3×2 supercells of SiX, respectively. E_{Li} is the Li-atom energy in the bulk bcc crystal, n is the number of adatoms adsorbed, and e symbolizes the electronic charge. The

average OCV was calculated to be 0.37 V for SiS and 0.32 V for SiSe. The OCV values are comparable to those of typically used commercial anode materials such as graphite (OCV = 0.2 V) and TiO$_2$ (1.5−1.8 V).[24]

To calculate the specific capacity, one must know the fully lithiated structure for SiS and SiSe. LiSiS ($x = 1$) and LiSiSe ($x = 1$) represent the fully lithiated structures, where 12 Li atoms reside at 12 different H$_1$ sites in a 3×2 supercell of SiS and SiSe. Further lithiation decreases the Li−Li distance significantly, thereby distorting the quasi-two-dimensional structures. The specific capacity can be evaluated as[65]

$$C_{\text{M}} = \frac{1}{M_{\text{SiX}}}(x_{\max}zF \times 10^3) \qquad (6)$$

where z represents the valence number ($z = 1$ for Li), F is the Faraday constant (26.810 A h/mol), and M_{SiX} is the atomic mass of the SiX system ($M_{\text{SiS}} = 60.15$ g/mol and $M_{\text{SiSe}} = 107.05$ g/mol). $x_{\max}$ represents the maximum number of Li atoms present per SiS or SiSe formula unit; in this case, $x_{\max} = 1$. Thus, the calculated specific capacities are 445.7 and 250.44

mA h g^{-1} for SiS and SiSe, respectively. The maximum capacity for SiS is similar to that for phosphorene (432.8 mA h g^{-1}). However, the higher atomic mass of Se makes the specific capacity comparatively lower for SiSe. Although the specific capacity of SiSe is lower than that of SiS or phosphorene, it is still higher than those of other commercial TiO_2- and Ti_3C_2-based anode materials.[24] In addition, SiSe undergoes very little structural distortion even at full lithiation and should therefore exhibit enhanced stability for charging/discharging cycles. Thus, their low operating voltages and moderate to high specific capacities make both SiS and SiSe manolayers promising anode materials for LIBs.

We investigated the electronic properties of pristine and lithiated silicon monosulfide/silicon monoselenide, to gain further insight into the binding mechanism of Li to these surfaces. The rate performance of the electrode is governed not only by the cation diffusion mechanism but also by the electron transport behavior. Figure 5 presents the band structures and densities of states (DOS) of pristine and fully lithiated SiS and SiSe. It was found that both pristine SiS (Figure 5a) and pristine SiSe (Figure 5c) are indirect-band-gap semiconductors with band gaps of 1.37 and 1.04 eV, respectively (at the PBE level), in line with previous theoretical calculations.[38,41] After complete lithiation (m = 12), it was observed that substantial electronic states appeared at the Fermi level and the band gap vanished, resulting in a semiconductor-to-metal transition for SiS (Figure 5b) and SiSe (Figure 5d). Phosphorene is also known to exhibit such quantum phase transition upon lithiation.[33] Large charge transfer from the 12 Li atoms to the SiS and SiSe monolayers assists in shifting the Fermi level into the conduction band, which eventually decreases the band gap. Such a semiconductor → metal transformation, therefore, ensures high electron mobility for these systems.

CONCLUSIONS

From first-principles, using density functional theory, we have explored the feasibility of using group IV monochalcogenide monolayers (SiS, SiSe, GeS, GeSe, SnS, and SnSe) as negative electrodes in Li-ion batteries. Our studies indicate that the Li binding energy to GeS, GeSe, SnS, and SnSe monolayers is low compared to the binding energy to SiS and SiSe monolayers. However, all of these values are well above the cohesive energy of lithium, showing their possible application as anode materials in LIBs. Although the adsorption energy of Li to SiS is highest in the series, SiSe also is predicted to have good Li binding capacity. Further calculations using SiS and SiSe monolayers revealed that Li diffusion over them exhibits a high anisotropy favoring diffusion along the zigzag direction with a low barrier of ~0.15 eV similar to the behavior of phosphorene. Inclusion of quantum effects for zero-point energy and tunneling enhance the diffusion rates by 6−10% at room temperature, which increases to as much as 40−60% at low temperatures (T = 100 K). The theoretical specific capacity was calculated to be 445.7 mA h g^{-1} for SiS monolayer and 250.44 mA h g^{-1} for SiSe monolayer, and the average open-circuit voltage lies in the appropriate experimental range of 0.32−0.36 V, similar to those of other commercially used anode materials. Upon full lithiation, these structures do not show any appreciable distortion and a semiconductor to metallic transformation ensures high electrical conductivity. All of these characteristics suggest that monolayer SiS and SiSe are indeed two promising candidates for designing negative electrodes in LIBs. Hence, synthesis of these materials through efficient deposition

technique is highly desirable for application in future energy technology.

ASSOCIATED CONTENT

Ⓢ Supporting Information

This material is available free of charge via the Internet. The Supporting Information is available free of charge on the ACS Publications website at DOI: 10.1021/acs.jpcc.6b04152.

Lithiated structures of SiS and SiSe at various Li concentrations (PDF)

AUTHOR INFORMATION

Corresponding Author

*E-mail: spad@iacs.res.in. Tel.: +91-0332473-4971.

Notes

The authors declare no competing financial interest.

REFERENCES

(1) Tarascon, J.-M. Key Challenges in Future Li-battery Research. *Philos. Trans. R. Soc., A* **2010**, *368*, 3227−3241.

(2) Etacheri, V.; Marom, R.; Elazari, R.; Salitra, G.; Aurbach, D. Challenges in the Development of Advanced Li-ion Batteries: A Review. *Energy Environ. Sci.* **2011**, *4*, 3243−3262.

(3) Tarascon, J.-M.; Armand, M. Issues and Challenges Facing Rechargeable Lithium Batteries. *Nature* **2001**, *414*, 359−367.

(4) Idota, Y.; Kubota, T.; Matsufuji, A.; Maekawa, Y.; Miyasaka, T. Tin-Based Amorphous Oxide: A High-Capacity Lithium-Ion-Storage Material. *Science* **1997**, *276*, 1395−1397.

(5) Yoo, E.; Kim, J.; Hosono, E.; Zhou, H.-s.; Kudo, T.; Honma, I. Large Reversible Li Storage of Graphene Nanosheet Families for Use in Rechargeable Lithium Ion Batteries. *Nano Lett.* **2008**, *8*, 2277−2282.

(6) Kang, B.; Ceder, G. Battery Materials for Ultrafast Charging and Discharging. *Nature* **2009**, *458*, 190−193.

(7) Xu, B.; Qian, D.; Wang, Z.; Meng, Y. S. Recent Progress in Cathode Materials Research for Advanced Lithium Ion Batteries. *Mater. Sci. Eng., R* **2012**, *73*, 51−65.

(8) Ji, L.; Lin, Z.; Alcoutlabi, M.; Zhang, X. Recent Developments in Nanostructured Anode Materials for Rechargeable Lithium-ion Batteries. *Energy Environ. Sci.* **2011**, *4*, 2682−2699.

(9) Armand, M.; Tarascon, J.-M. Building Better Batteries. *Nature* **2008**, *451*, 652−657.

(10) Noel, M.; Suryanarayanan, V. Role of Carbon Host Lattices in Li-Ion Intercalation/De-intercalation Processes. *J. Power Sources* **2002**, *111*, 193−209.

(11) Nitta, N.; Wu, F.; Lee, J. T.; Yushin, G. Li-ion Battery Materials: Present and Future. *Mater. Today* **2015**, *18*, 252−264.

(12) Kaskhedikar, N. A.; Maier, J. Lithium Storage in Carbon Nanostructures. *Adv. Mater.* **2009**, *21*, 2664−2680.

(13) Liang, M.; Zhi, L. Graphene-based Electrode Materials for Rechargeable Lithium Batteries. *J. Mater. Chem.* **2009**, *19*, 5871−5878.

(14) Fan, X.; Zheng, W.; Kuo, J.-L.; Singh, D. J. Adsorption of Single Li and the Formation of Small Li Clusters on Graphene for the Anode of Lithium-ion batteries. *ACS Appl. Mater. Interfaces* **2013**, *5*, 7793−7797.

(15) Hatchard, T.; Dahn, J. In Situ XRD and Electrochemical Study of the Reaction of Lithium with Amorphous Silicon. *J. Electrochem. Soc.* **2004**, *151*, A838−A842.

(16) Chan, C. K.; Peng, H.; Liu, G.; McIlwrath, K.; Zhang, X. F.; Huggins, R. A.; Cui, Y. High-performance Lithium Battery Anodes Using Silicon Nanowires. *Nat. Nanotechnol.* **2008**, *3*, 31−35.

(17) Kasavajjula, U.; Wang, C.; Appleby, A. J. Nano-and Bulk-silicon-based Insertion Anodes for Lithium-ion Secondary Cells. *J. Power Sources* **2007**, *163*, 1003−1039.

(18) Zhao, K.; Wang, W. L.; Gregoire, J.; Pharr, M.; Suo, Z.; Vlassak, J. J.; Kaxiras, E. Lithium-assisted Plastic Deformation of Silicon Electrodes in Lithium-ion Batteries: A First-principles Theoretical Study. *Nano Lett.* **2011**, *11*, 2962−2967.

(19) Jose, D.; Datta, A. Understanding of the Buckling Distortions in Silicene. *J. Phys. Chem. C* **2012**, *116*, 24639−24648.

(20) Jose, D.; Datta, A. Structures and Chemical Properties of Silicene: Unlike Graphene. *Acc. Chem. Res.* **2014**, *47*, 593−602.

(21) Ivanov, A. S.; Bozhenko, K. V.; Boldyrev, A. I. On the Suppression Mechanism of the Pseudo-Jahn−Teller Effect in Middle E_6 (E = P, As, Sb) Rings of Triple-Decker Sandwich Complexes. *Inorg. Chem.* **2012**, *51*, 8868−8872.

(22) Tritsaris, G. A.; Kaxiras, E.; Meng, S.; Wang, E. Adsorption and Diffusion of Lithium on Layered Silicon for Li-ion Storage. *Nano Lett.* **2013**, *13*, 2258−2263.

(23) Zhu, J.; Chroneos, A.; Schwingenschlögl, U. Silicene/Germanene on MgX 2 (X= Cl, Br, and I) for Li-ion Battery Applications. *Nanoscale* **2016**, *8*, 7272−7277.

(24) Tang, Q.; Zhou, Z.; Shen, P. Are MXenes Promising Anode Materials for Li Ion Batteries? Computational Studies on Electronic Properties and Li Storage Capability of Ti3C2 and Ti3C2 × 2 (X= F, OH) Monolayer. *J. Am. Chem. Soc.* **2012**, *134*, 16909−16916.

(25) Chen, H. J.; Huang, J.; Lei, X. L.; Wu, M. S.; Liu, G.; Ouyang, C. Y.; Xu, B. Adsorption and Diffusion of Lithium on MoS2 Monolayer: The Role of Strain and Concentration. *Int. J. Electrochem. Sci.* **2013**, *8*, 2196−2203.

(26) Yang, L.-M.; Bačić, V.; Popov, I. A.; Boldyrev, A. I.; Heine, T.; Frauenheim, T.; Ganz, E. Two-Dimensional Cu2Si Monolayer with Planar Hexacoordinate Copper and Silicon Bonding. *J. Am. Chem. Soc.* **2015**, *137*, 2757−2762.

(27) Yang, L.-M.; Popov, I. A.; Boldyrev, A. I.; Heine, T.; Frauenheim, T.; Ganz, E. Post-anti-van't Hoff-Le Bel Motif in Atomically Thin Germanium−Copper Alloy Film. *Phys. Chem. Chem. Phys.* **2015**, *17*, 17545−17551.

(28) Yang, L.-M.; Popov, I. A.; Frauenheim, T.; Boldyrev, A. I.; Heine, T.; Bačić, V.; Ganz, E. Revealing Unusual Chemical Bonding in Planar Hyper-Coordinate Ni2Ge and Quasi-planar Ni2Si Two-Dimensional Crystals. *Phys. Chem. Chem. Phys.* **2015**, *17*, 26043−26048.

(29) Chowdhury, C.; Jahiruddin, S.; Datta, A. Psuedo Jahn−Teller Distortion in Two-Dimensional Phosphorus: Origin of Black and Blue Phases of Phosphorene and Band Gap Modulation by Molecular Charge Transfer. *J. Phys. Chem. Lett.* **2016**, *7*, 1288−1297.

(30) Park, C. M.; Sohn, H. J. Black Phosphorus and Its Composite for Lithium Rechargeable Batteries. *Adv. Mater.* **2007**, *19*, 2465−2468.

(31) Sun, J.; Lee, H.-W.; Pasta, M.; Yuan, H.; Zheng, G.; Sun, Y.; Li, Y.; Cui, Y. A Phosphorene−graphene Hybrid Material as a High-capacity Anode for Sodium-ion Batteries. *Nat. Nanotechnol.* **2015**, *10*, 980−985.

(32) Sun, J.; Zheng, G.; Lee, H.-W.; Liu, N.; Wang, H.; Yao, H.; Yang, W.; Cui, Y. Formation of Stable Phosphorus−Carbon Bond for Enhanced Performance in Black Phosphorus Nanoparticle−graphite Composite Battery Anodes. *Nano Lett.* **2014**, *14*, 4573−4580.

(33) Zhao, S.; Kang, W.; Xue, J. The Potential Application of Phosphorene as an Anode Material in Li-ion Batteries. *J. Mater. Chem. A* **2014**, *2*, 19046−19052.

(34) Guo, G.-C.; Wang, D.; Wei, X.-L.; Zhang, Q.; Liu, H.; Lau, W.-M.; Liu, L.-M. First-Principles Study of Phosphorene and Graphene Heterostructure as Anode Materials for Rechargeable Li Batteries. *J. Phys. Chem. Lett.* **2015**, *6*, 5002−5008.

(35) Wang, G.; Slough, W. J.; Pandey, R.; Karna, S. P. Degradation of Phosphorene in Air: Understanding at Atomic Level. *2D Mater.* **2016**, *3*, 025011.

(36) Chowdhury, C.; Karmakar, S.; Datta, A. Capping Black Phosphorene by h-BN Enhances Performances in Anodes for Li and Na Ion Batteries. *ACS Energy Lett.* **2016**, *1*, 253−259.

(37) Gomes, L. C.; Carvalho, A. Phosphorene Analogues: Isoelectronic Two-dimensional Group-IV Monochalcogenides with Orthorhombic Structure. *Phys. Rev. B: Condens. Matter Mater. Phys.* **2015**, *92*, 085406.

(38) Zhu, Z.; Guan, J.; Liu, D.; Tománek, D. Designing Isoelectronic Counterparts to Layered Group V Semiconductors. *ACS Nano* **2015**, *9*, 8284−8290.

(39) Brent, J. R.; Lewis, D. J.; Lorenz, T.; Lewis, E. A.; Savjani, N.; Haigh, S. J.; Seifert, G.; Derby, B.; O'Brien, P. Tin (II) Sulfide (SnS) Nanosheets by Liquid-Phase Exfoliation of Herzenbergite: IV−VI Main Group Two-Dimensional Atomic Crystals. *J. Am. Chem. Soc.* **2015**, *137*, 12689−12696.

(40) Chang, Y.-H.; Zhang, W.; Zhu, Y.; Han, Y.; Pu, J.; Chang, J.-K.; Hsu, W.-T.; Huang, J.-K.; Hsu, C.-L.; Chiu, M.-H.; et al. Monolayer MoSe2 Grown by Chemical Vapor Deposition for Fast Photo-detection. *ACS Nano* **2014**, *8*, 8582−8590.

(41) Mehboudi, M.; Dorio, A. M.; Zhu, W.; van der Zande, A.; Churchill, H. O.; Pacheco-Sanjuan, A. A.; Harriss, E. O.; Kumar, P.; Barraza-Lopez, S. Two-dimensional Disorder in Black Phosphorus and Monochalcogenide Monolayers. *Nano Lett.* **2016**, *16*, 1704−1712.

(42) Im, H. S.; Lim, Y. R.; Cho, Y. J.; Park, J.; Cha, E. H.; Kang, H. S. Germanium and Tin Selenide Nanocrystals for High-Capacity Lithium Ion Batteries: Comparative Phase Conversion of Germanium and Tin. *J. Phys. Chem. C* **2014**, *118*, 21884−21888.

(43) Vaughn, D. D.; Hentz, O. D.; Chen, S.; Wang, D.; Schaak, R. E. Formation of SnS Nanoflowers for Lithium Ion Batteries. *Chem. Commun.* **2012**, *48*, 5608−5610.

(44) Hang, B. T.; Ohnishi, T.; Osada, M.; Xu, X.; Takada, K.; Sasaki, T. Lithium Silicon Sulfide as an Anode Material in All-solid-state Lithium Batteries. *J. Power Sources* **2010**, *195*, 3323−3327.

(45) Carpenter, B. K. Heavy-Atom Tunneling as the Dominant Pathway in a Solution-Phase Reaction? Bond Shift in Antiaromatic Annulenes. *J. Am. Chem. Soc.* **1983**, *105*, 1700−1701.

(46) Datta, A.; Hrovat, D. A.; Borden, W. T. Calculations Predict Rapid Tunneling by Carbon from the Vibrational Ground State in the Ring Opening of Cyclopropylcarbinyl Radical at Cryogenic Temperatures. *J. Am. Chem. Soc.* **2008**, *130*, 6684−6685.

(47) Zuev, P. S.; Sheridan, R. S.; Albu, T. V.; Truhlar, D. G.; Hrovat, D. A.; Borden, W. T. Carbon Tunneling from a Single Quantum State. *Science* **2003**, *299*, 867−870.

(48) Wigner, E. The Transition State Method. *Trans. Faraday Soc.* **1938**, *34*, 29−41.

(49) Wigner, E. P. On Crossing Over Potential Barriers in Chemical Reactions. *Z. Phys. Chem., Abt. B* **1932**, *19*, 203.

(50) Giannozzi, P.; Baroni, S.; Bonini, N.; Calandra, M.; Car, R.; Cavazzoni, C.; Ceresoli, D.; Chiarotti, G. L.; Cococcioni, M.; Dabo, I.; et al. Quantum ESPRESSO: A Modular and Open-Source Software Project for Quantum Simulations of Materials. *J. Phys.: Condens. Matter* **2009**, *21*, 395502.

(51) Vanderbilt, D. Soft Self-Consistent Pseudopotentials in a Generalized Eigenvalue Formalism. *Phys. Rev. B: Condens. Matter Mater. Phys.* **1990**, *41*, 7892.

(52) Perdew, J. P.; Burke, K.; Ernzerhof, M. Generalized Gradient Approximation Made Simple. *Phys. Rev. Lett.* **1996**, *77*, 3865.

(53) Broyden, C. G. The Convergence of a Class of Double-rank Minimization Algorithms 2. The New Algorithm. *IMA. J. Appl. Math.* **1970**, *6*, 222−231.

(54) Grimme, S. Semiempirical GGA-type Density Functional Constructed with a Long-range Dispersion Correction. *J. Comput. Chem.* **2006**, *27*, 1787−1799.

(55) Henkelman, G.; Jónsson, H. Improved Tangent Estimate in the Nudged Elastic Band Method for Finding Minimum Energy Paths and Saddle Points. *J. Chem. Phys.* **2000**, *113*, 9978−9985.

(56) Sanville, E.; Kenny, S. D.; Smith, R.; Henkelman, G. Improved Grid-based Algorithm for Bader Charge Allocation. *J. Comput. Chem.* **2007**, *28*, 899−908.

(57) Kresse, G.; Joubert, D. From Ultrasoft Pseudopotentials to the Projector Augmented-wave Method. *Phys. Rev. B: Condens. Matter Mater. Phys.* **1999**, *59*, 1758.

(58) Kresse, G.; Furthmüller, J. Efficient Iterative Schemes for Ab-initio Total-energy Calculations Using a Plane-wave Basis Set. *Phys. Rev. B: Condens. Matter Mater. Phys.* **1996**, *54*, 11169.

(59) Kaxiras, E. *Atomic and Electronic Structure of Solids*; Cambridge University Press: Cambridge, U.K., 2003.

(60) Karmakar, S.; Datta, A. Tunneling Assists the 1, 2-Hydrogen Shift in N-Heterocyclic Carbenes. *Angew. Chem., Int. Ed.* **2014**, *53*, 9587−9591.

(61) Karmakar, S.; Datta, A. Role of Quantum Mechanical Tunneling on the γ-Effect of Silicon on Carbenes in 3-Trimethylsilylcyclobuty-lidene. *J. Phys. Chem. B* **2014**, *118*, 2553−2558.

(62) Karmakar, S.; Datta, A. Role of Heavy Atom Tunneling in Myers-Saito Cyclization of Cyclic Enyne-Cumulene Systems. *J. Phys. Chem. B* **2016**, *120*, 945−950.

(63) Dixit, M.; Kosa, M.; Lavi, O. S.; Markovsky, B.; Aurbach, D.; Major, D. T. Thermodynamic and kinetic studies of Li-$Ni_{0.5}Co_{0.2}Mn_{0.3}O_2$ as a positive electrode material for Li-ion batteries using first principles. *Phys. Chem. Chem. Phys.* **2016**, *18*, 6799−6812.

(64) Henkelman, G.; Arnaldsson, A.; Jónsson, H. Theoretical Calculations of CH_4 and H_2 Associative Desorption from Ni(111) Could Subsurface Hydrogen Play an Important Role? *J. Chem. Phys.* **2006**, *124*, 044706-1−044706-9.

(65) Er, D.; Li, J.; Naguib, M.; Gogotsi, Y.; Shenoy, V. B. Ti3C2MXene as a High Capacity Electrode Material for Metal (Li, Na, K, Ca) Ion Batteries. *ACS Appl. Mater. Interfaces* **2014**, *6*, 11173−11179.